Finite Element Based Improved Characterization of Viscoelastic Materials

Xianfeng Song[1*], Stefan Dircks[1], Daniil Mirosnikov[1], and Benny Lassen[2]

[1] *Mads Clausen Institute, SDU, Sønderborg, Denmark*
[2] *DONG Energy, Fredericia, Denmark*

[*] *SDU, Alsion 2, 6400, Sønderborg, Denmark, sxf19911101@gmail.com*

Abstract: The objective of this study is to acquire a full characterization of a hyperelastic material. The process is realized by performing a Dynamic Mechanical Analysis (DMA) while simultaneously extending it by advanced image processing algorithms in order to measure the changing distance in the contracting direction. Using COMSOL's weak form PDE physics interface, three mathematical models are developed, where the strain-energy density function depends on different hyperelastic constitutive equations. The chosen constitutive equations are Mooney-Rivlin, Yeoh and Arruda-Boyce. The results of the numerical study demonstrate that the all three models exhibit the correct trend of the non-linear behavior of the material, while the Arruda-Boyce model shows the best fitting performance.

Keywords: finite element method, COMSOL, viscoelastic material, image processing, dynamic mechanical analysis

I. Introduction

Viscoelastic materials have been used in many different applications, for example isolating vibration, dampening noise and absorbing shock. Synthetic polymers, wood, and human tissue, as well as metals at high temperature, display significant viscoelastic effects [1]. Viscoelastic materials exhibit several non-trivial effects such as highly non-linear dynamic behavior. When an elastic material is deformed due to an applied external force, internal resistance counters the deformation and restores it to its original state if the external force is no longer applied [2], [3]. In general, it is inherently complex to model behaviors of such materials using a finite element software due to its non-linear properties. This paper describes the full characterization of a viscoelastic material. The acquired experimental results, from DMA and advanced image processing, are subsequently implemented in the finite element software for developing an optimized model of the material.

The image processing algorithms are developed using *MATLAB version R2015a*. The optimization and development of the final model of the material is performed in the finite element analysis, solver and simulation software - *COMSOL Multiphysics version 5.1*.

II. Theory

For the given material, linear elastic models (e.g. Neo-Hookean model) can not accurately describe the observed behavior, so in order to overcome this problem hyperelastic material models are introduced. Hyperelasticity provides a means of modeling the stress-strain behavior of such materials [4].

In this section a derivation of the governing equation is given. This theoretical part is required in order to perform a finite element analysis.

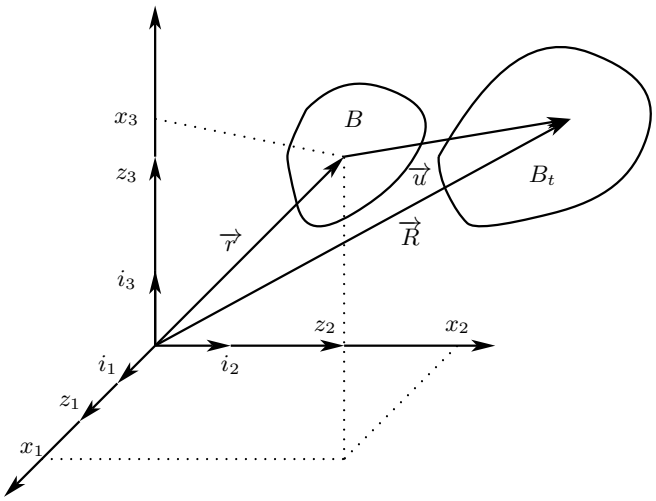

Fig. 1. General coordinate system with deformed and undeformed bodies.

Figure 1 graphically represents the general coordinate system where $\vec{i_1}$, $\vec{i_2}$ and $\vec{i_3}$ are the three unit normal vectors. The projection of the undeformed body with volume B is represented by positions x_1, x_2 and x_3 on the general coordinate system, while the projection of the deformed body with volume B_t is represented by positions z_1, z_2 and z_3.

The position vector from the origin $(0, 0, 0)$ to a certain point in the undeformed body is denoted by $\vec{r}$:

$$\vec{r} = \sum_{i=1}^{3} x_i \vec{i_i} = x_i \vec{i_i}, \tag{1}$$

where the latter term denotes Einsteins summation convention, used throughout the entire paper. The corresponding position after deformation of the body is given

by $\overrightarrow{R}$.

$$\overrightarrow{R} = z_i \overrightarrow{i_i}. \tag{2}$$

In addition the displacement $\overrightarrow{u}$ is given as

$$\overrightarrow{u} = \overrightarrow{R} - \overrightarrow{r}. \tag{3}$$

Hamilton's Principle:
Hamilton's principle is used to derive the governing equation for the deformation of the viscoelastic material. The action integral is defined as

$$I = \int_{t_1}^{t_2} L dt, \tag{4}$$

where L is the Lagrangian which is defined as the difference between the kinetic and potential energy:

$$L = T - W, \tag{5}$$

where T is the kinetic energy and W is the potential energy. In the undeformed configuration (reference configuration) we have:

$$T = \int_B \frac{1}{2} \rho_R \overrightarrow{v}^2 dB, \tag{6}$$

where B is the undeformed volume, $\overrightarrow{v}$ is the velocity and ρ_R the reference mass density.
The potential energy W is given by:

$$W = \int_B \rho_R e dB, \tag{7}$$

where e is the deformation energy density, which depends on the deformation gradient F:

$$e = e(F), \tag{8}$$

with

$$F_{ij} = \frac{\partial z_i}{\partial x_j} = \frac{\partial u_i}{\partial x_j} + \delta_{ij}. \tag{9}$$

Finding the first variation of the action integral leads to the governing equation

$$\delta I = \int_{t_1}^{t_2} \int_B \left(\rho_R \frac{\partial u_i}{\partial t} \frac{\partial \delta u_i}{\partial t} - \delta W \right) dB dt. \tag{10}$$

Equation (7) is the accurate representation of the potential energy, but due to its non-linearity, it is too complex to find the expression for the strain energy density function. Therefore the potential energy W is expressed as one of the hyperelastic constitutive models. In this case the potential energy is expressed by Mooney-Rivlin [5] [6], Yeoh [7] [8] and Arruda-Boyce [9] [10] hyperelastic models.

1) Mooney-Rivlin Model:

$$W = C_{01}(\bar{I}_2 - 3) + C_{10}(\bar{I}_1 - 3) + D_1(J-1)^2, \tag{11}$$

where C_{01}, C_{10} and D_1 are material parameters.

2) Yeoh Model:

$$W = \sum_{i=1}^{n} C_{i0}(\bar{I}_1 - 3)^i + \sum_{k=1}^{n} C_{k1}(J-1)^{2k}, \tag{12}$$

where C_{i0} and C_{k1} are material parameters, and we choose $n = 2$ in order to reduce the time to perform parameter estimation. Moreover, by increasing n will not give significantly more accurate results.

3) Arruda-Boyce Model:

$$W = D_1 \left(\frac{J^2 - 1}{2} - \ln J \right) + C_1 \sum_{i=1}^{5} \alpha_i \beta^{i-1} (\bar{I}_1^i - 3^i), \tag{13}$$

where D_1, C_1 and β are the optimized parameters and $\beta := \frac{1}{N}$, $\alpha_1 := \frac{1}{2}$, $\alpha_2 := \frac{1}{20}$, $\alpha_3 := \frac{11}{1050}$, $\alpha_4 := \frac{19}{7000}$ and $\alpha_5 := \frac{519}{673750}$.

Note that

$$\bar{I}_1 = J^{-2/3} I_1, \tag{14}$$

$$\bar{I}_2 = J^{-4/3} I_2, \tag{15}$$

$$J = det(F), \tag{16}$$

where I_1 and I_2 are the first and the second invariant of the unimodular component of the left Cauchy-Green deformation tensor.

In order to compare with the DMA experiments results, it is needed to calculate the generated force on the lower surface, shown in Figure 2.

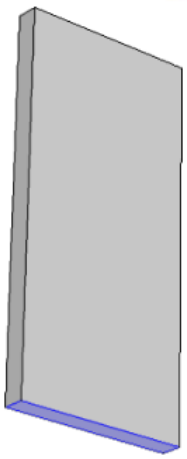

Fig. 2. The time-dependent lower boundary condition.

The force is given by

$$F = \int_{A_t} T_{ij} n_j dS_t = \int_A S_{ij} N_j dS, \tag{17}$$

where A_t is the surface area in the deformed configuration and A is the surface area in the undeformed configuration. It is of less complexity to calculate the force in the

undeformed configuration. According to the first Piola Kirchhoff stress

$$S_{ij} = \rho_R \frac{\partial e}{\partial F_{ij}}, \tag{18}$$

since

$$W = \rho_R e \tag{19}$$

equation (18) can be re-written into

$$S_{ij} = \frac{\partial W}{\partial F_{ij}}. \tag{20}$$

Combining equation (17) and (20) will give the force F. Then it is possible to calculate the error between the measured and simulated forces.

III. Experimental Results

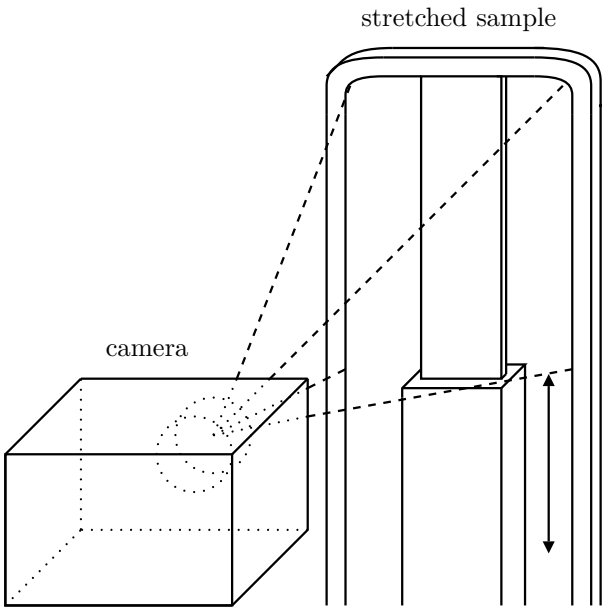

Fig. 3. Schematic setup of the dynamic mechanical analysis with image processing extension. The mounted *Go Pro Hero 4 Black* aims the sample on the right side.

After performing the test, graphically shown in Figure 3, the acquired results are illustrated in Figure 4. The resultant force-displacement graph demonstrates the material non-linearity. Therefore it is essential to implement a hyperelastic model of higher order. Figure 5 illustrates the obtained results from image processing. The Fig. 5 (a) shows the initial position of the detected dots where the material is undeformed. On the other side Figure 5 (b) shows the final position, when the sample is under deformation. Figure 6 represents the distance between the left and right dots and how it changes over the time of the video. As it can be seen, the distance between the dots decreases as the material is being stretched. This behavior is expected due to the fact that the middle part contracts when the material is being stretched.

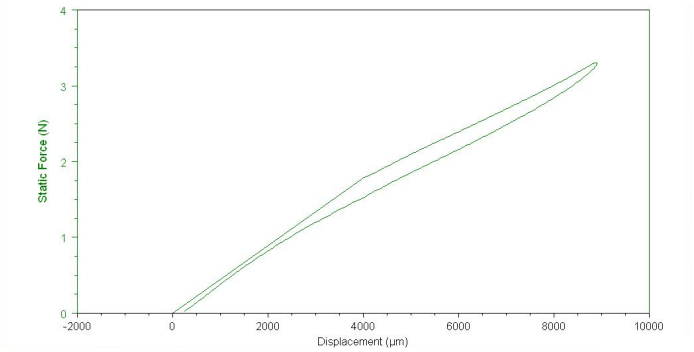

Fig. 4. The result of force vs. displacement, where one can see from this hysteresis that the displacement and the force are non-linear.

(a) On this figure the detection aims the left and the right dot, respectively. The sample is unstretched.

(b) The final frame where the sample is stretched. Again the code detects the left and the right dot, respectively.

Fig. 5. The results of the image processing. The two figures on the left represents the unstretched sample and the two figure on the right represents the stretched sample.

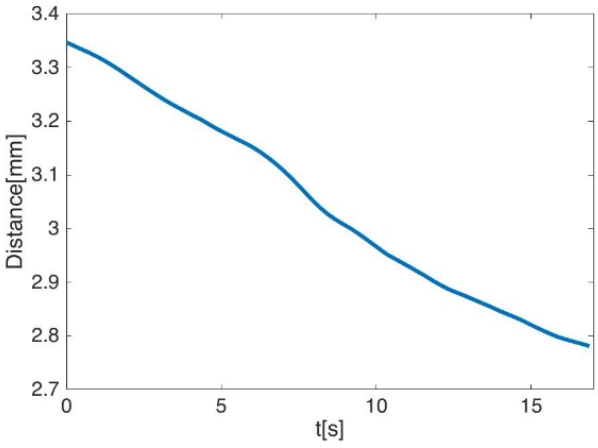

Fig. 6. Distance between the left and right dots vs. Time. As the material is being stretched the distance between the dots reduces.

IV. COMSOL Implementation

Model Building

This model is built in a three dimensional space using time-dependent weak form PDE. The geometry of the model, graphically represented in Figure 7, is based on sample dimensions, including the painted dots which are placed by using domain point probes.

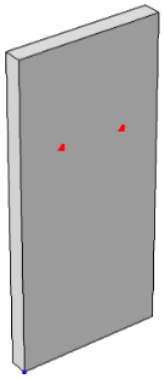

Fig. 7. Geometry model including two probes. The probes placements corresponds to the position of the painted dots of the real sample.

The previous derived governing equation (10) is implemented in *weak form PDE* weak expression:

$$rho * (d(u1,t) * d(test(u1),t) + d(u2,t) * d(test(u2),t) + d(u3,t) * d(test(u3),t)) - test(W)$$

The strain energy density function W is expressed depending on the chosen hyperelastic model.

W	C1*(I1_h-3)+D1*(J-1)^2
C11	F11^2+F21^2+F31^2
C12	F11*F12+F21*F22+F31*F32
C13	F11*F13+F21*F23+F31*F33
C21	C12
C22	F12^2+F22^2+F32^2
C23	F12*F13+F22*F23+F32*F33
C31	C13
C32	C23
C33	F13^2+F23^2+F33^2

Fig. 8. Implementation of Mooney-Rivlin hyper elastic model in variables.

The upper boundary is allowed to move in the z-direction. The prescribed value is set to be the linear interpolation of the change of length of the real sample (measured by the *DMA*).

In order to perform optimization, the error between the measured data and modeled data needs to be calculated:

$$E_1 = \int_0^T (F - F_{\text{measured}})^2 dt, \tag{21}$$

$$E_2 = \int_0^T (D - D_{\text{image processing}})^2 dt, \tag{22}$$

$$E = \alpha_1 E_1 + \alpha_2 E_2, \tag{23}$$

where E_1, E_2 and E are the error between the simulated and measured force, error between the simulated and image processing distances and the total error, respectively. In addition, α_1 and α_2 are weighting values. The challenge of solving time dependent integrals in *COMSOL* is circumvented by manually differentiating equation (23) and solving it by using the physics *Global ODEs and DAEs*:

$$\frac{dE}{dt} - \alpha_1 \frac{dE_1}{dt} - \alpha_2 \frac{dE_2}{dt} = 0. \tag{24}$$

The Nelder-Mead method is used to minimize the integral of the total error, which is done by optimizing the control variables, which depend on the hyperelastic model.

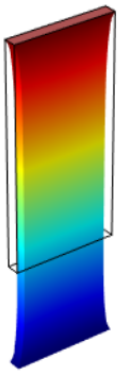

(a) The resultant deformation shown in 3D.

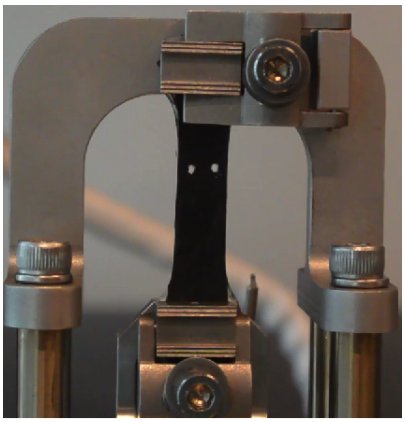

(b) The stretched material sample.

Fig. 9. The stretched material sample results. It shows a comparison between the simulated and the DMA results.

V. Numerical Results

In this section the acquired results are demonstrated and compared with each other. Figure 9 (a) graphically represents the resultant deformation of the sample at the end of the test. The shape of this simulated deformation fits with the sample, observed during the *DMA* (shown in Figure 9 (b)). Figure 10 (a) illustrates the comparison of the measured and simulated forces using the Mooney-Rivlin hyperelastic model. In the first 9 seconds it can be seen that the error does not exceed 3% but globally the model follows the measured data. In addition a comparison between the distances of the model and image processing is represented in Figure 10 (b). The second model is the Yeoh hyperelastic model. The results are represented in Figure 11 (a) and 11 (b). Comparing the graphs of force vs. time of the Yeoh model and the Mooney-Rivlin model it can be seen that both models behave in a similar way. However by comparing the distance between their dots it can be noticed that even though the resultant shapes are similar, the biggest error in the Yeoh model is smaller.

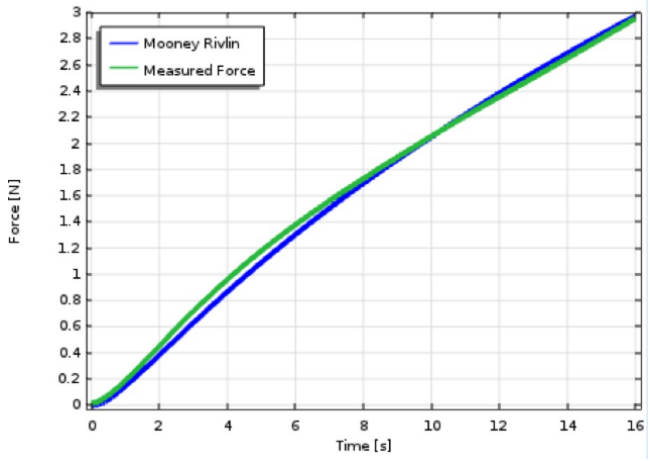

(a) Force comparison using Mooney-Rivlin hyperelasic model.

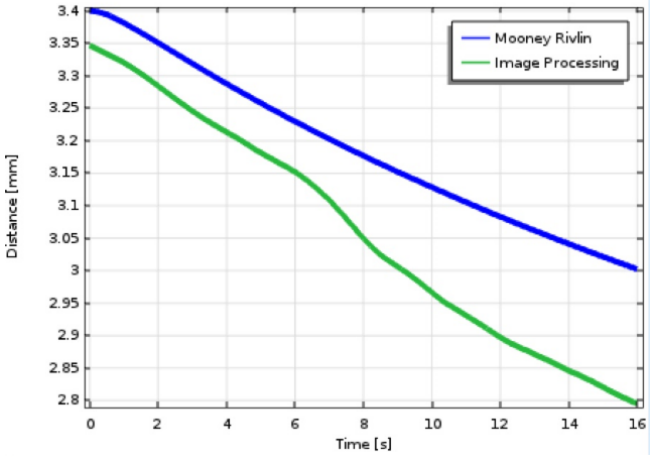

(b) Comparison of distances between the created two dots.

Fig. 10. The Mooney-Rivlin hyperelastic model results.

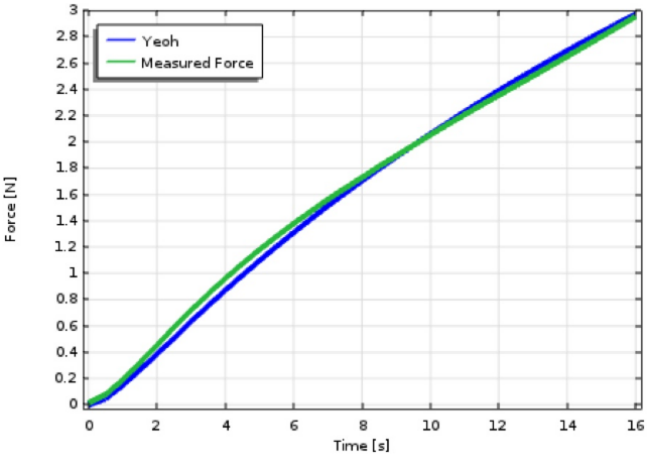

(a) Comparison of measured and simulated forces by applying Yeoh method.

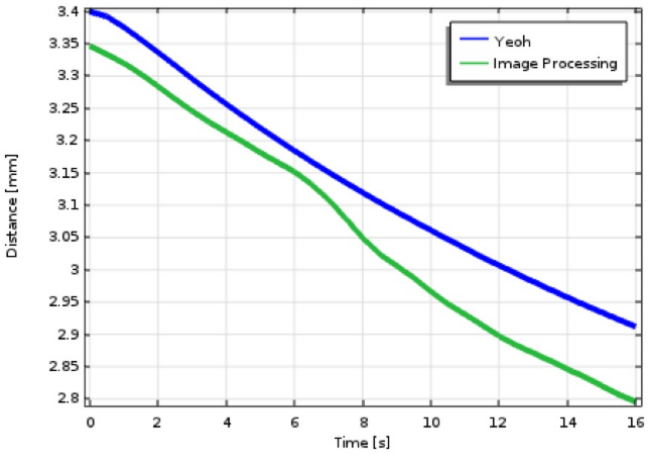

(b) Comparison of measured and simulated distances between two dots by applying Yeoh method.

Fig. 11. The Yeoh hyperelastic model results.

The last model is chosen to be the Arruda-Boyce model. The results, graphically represented in Fig. 12 (a) and 12 (b), shows the best fitting of the simulated model to the real model. As it can be seen on the distance between two dots vs. time graph, the biggest error is three times smaller if compared to the Yeoh model and four times smaller to the Mooney-Rivlin model.

VI. Conclusion

From the results of the DMA test it can be concluded that the material exhibits non-linear behavior between the force and the displacement. It can also be seen, that the material has hysteresis properties.
Due to the unstable frame rate of the used camera and its limited resolution, the error in the image processing algorithms should be improved in future development.
From the results of the *COMSOL* simulations, all of the hyperelastic models exhibit the correct trend of the non-

linear behavior of the material. However, the Arruda-Boyce hyperelastic material model proves to be the most accurate of the chosen.

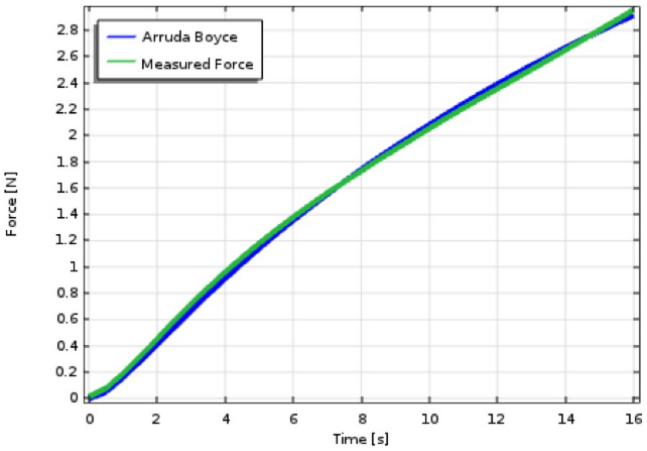

(a) Force comparison using Arruda-Boyce hyperelastic model.

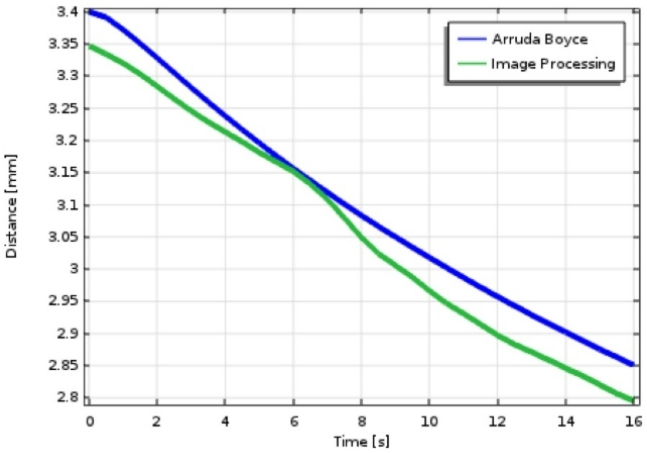

(b) Comparison of measured and simulated distances between two dots by applying Arruda-Boyce hyperelastic model.

Fig. 12. The Arruda-Boyce hyperelastic model results.

References

[1] Sorbothane, "The Difference Between Elastic Materials and Viscoelastic Materials" http://www.sorbothane.com/the-difference-between-elastic-materials-and-viscoelastic-materials.aspx, 2015, Accessed December 15, 2015.

[2] M. Meyers, K. Chawla, *Mechanical Behavior of Materials (2nd Edition)*, page 71. Prentice Hall, 1999.

[3] L. D. Landau, E. M. Lifshitz, *Theory of Elasticity*. A Course of Theoretical Physics Vol. 7 (2nd Edition), page 1970.

[4] A. H. Muhr, *Modeling the stres-strain behavior of rubber*. Rubber chemistry and technology, 78(3), p. 391-425, 2005.

[5] M. Mooney, *A theory of large elastic deformation*. Journal of Applied Physics, 11(9), pp. 582-592, 1940.

[6] R. S. Rivlin, *Large elastic deformations of isotropic materials*. IV. Further developments of the general theory, Philosophical Transactions of the Royal Society of London. Series A, Mathematical and Physical Sciences, 241(835), pp. 379-397, 1948.

[7] O. H. Yeoh, *Some forms of the strain energy function for rubber*. Rubber Chemistry and technology, Volume 66, Issue 5, November 1993, pp. 754-771, 1993.

[8] R. S. Rivlin, *Some applications of elasticity theory to rubber engineering*. Collected Papers of R. S. Rivlin vol. 1 and 2, Springer, 1997.

[9] E. M. Arruda, M. C. Boyce, *A three-dimensional model for the large stretch behavior of rubber elastic materials*. J. Mech. Phys. Solids, 41(2), pp. 389–412, 1993.

[10] M. Kaliske, H. Rothert, *On the finite element implementation of rubber-like materials at finite strains*. Engineering Computations, 14(2), pp. 216–232, 1997.

[11] X. Yang, *Engineering Optimization: An Introduction with Metaheuristic Applications (1st Edition*. Page 86, Wiley, 2010.